Synthesis and Photoluminescent Properties of Rare Earth Doped ZnO Hierarchical Microspheres

Xiaoyan Zeng,* Junlin Yuan,[†] and Lide Zhang*

Key Laboratory of Materials Physics, Institute of Solid State Physics, Chinese Academy of Sciences, P.O. Box 1129, Hefei 230031, P. R. China

Received: August 24, 2007; In Final Form: December 11, 2007

Hierarchical ZnO microspheres constructed by mesoporous quasi-single-crystalline ZnO nanosheets were fabricated by pyrolysis of the microspheres of layered hydroxide zinc carbonate, $Zn_5(CO_3)_2(OH)_6$, which was the hydrothermal precipitate of zinc nitrate and urea. A growth mechanism of $Zn_5(CO_3)_2(OH)_6$ microspheres was proposed. During the pyrolysis process, single-crystalline $Zn_5(CO_3)_2(OH)_6$ nanosheets were transformed into mesoporous quasi-single-crystalline ZnO nanosheets. When the samples were doped with trivalent rare earth ion, RE^{3+} (RE = Pr, Sm, Tb, Ho, Tm), no ZnO $\rightarrow$ RE^{3+} energy transfer was observed. However, the ZnO:Eu^{3+} sample showed efficient Eu^{3+} emissions under UV photon excitation (λ < 365 nm), which is attributed to energy transfer from photon-generated electron−hole pairs to Eu^{3+} ions in the surface layer of the ZnO nanosheet.

1. Introduction

The arrangement of micro- and nanostructured building blocks into hierarchical structures is of great interest to chemists and materials scientists.[1] Zinc oxide, of which the band gap is 3.37 eV and exciton binding energy is 60 meV, is interesting to study not only because of the recent demonstrations of unique physical properties such as UV lasing emission and photoconductivity properties[2] in nanowire form but also because a wide variety of morphologies have been prepared, of which the optical properties are related to the morphologies.[3] Great efforts have been devoted to the development of synthetic methodologies for ZnO nanocrystals, such as CVD, laser irradiation, and hydrothermal method. Among these methods, hydrothermal method is a promising method that is efficient, cost-effective, and easy to manipulate.[4]

On the other side, trivalent rare earth doped semiconductors such as GaN:RE and Si:Er are technologically important materials in optoelectric devices and have received great research interest,[5] in which an efficient energy transfer from semiconductor host to RE^{3+} ions is essential for most of the potential applications. In the systems of RE^{3+}-doped ZnO, most of the studies are focused on Eu^{3+} doping. However, the doping of Eu^{3+} into ZnO lattice remains disappointing[6] and could be attributed to two difficulties. The first one is the low saturated concentration of rare earth ion in ZnO lattice due to the large differences in ionic size and charge between Eu^{3+} (r = 94.7 pm, CN = 6) and Zn^{2+} (r = 60 pm, CN = 4).[7] The second difficulty is the inappropriate energy level position of rare earth ion relative to the valence band and conduction band of ZnO host. Dorenbos and van der Kolk pointed out that the charge-transfer level of Eu^{3+} in ZnO is equal or higher than the bottom of conduction band of ZnO, which leads to the absence of efficient ZnO $\rightarrow$ Eu^{3+} energy transfer.[8] Since optical properties of semiconductor nanostructures are related to the surface states,

using hydrothermal method it is possible to synthesize novel nanostructures of ZnO with appropriate surface states that favor energy transfer from ZnO to rare earth ions.

2. Experimental Section

Synthesis. All reagents used in the experiment were of analytical grade. The detailed synthesis procedures were described as follows. Rare earth oxides were dissolved in diluted HNO_3 solution, heated to dryness at 120 °C, and added with deionized water to form 0.02 M $RE(NO_3)_3$ solutions. $Zn(NO_3)_2 \cdot 6H_2O$ (0.0009−0.027 mol) and urea (0.009−0.09 mol) were weighed and added in deionized water to form 45 mL of aqueous clear solutions. For rare earth doped samples, the 0.02 M rare earth nitrate solutions were also added. The mixture solutions were stirred continuously until all the reagents were dissolved completely, and the starting pH values were 5 to 6. The mixed solutions were poured into Teflon-lined autoclaves (60 mL), sealed, and held at 120 °C for 1−24 h. After that, the autoclaves were cooled to room temperature naturally (final pH value of 9), and the precipitates at the bottom of the autoclaves were collected by centrifugation, washed using absolute ethanol and deionized water, and finally dried in air at 60 °C. The hydrothermal products were converted to ZnO phase by subsequent annealing in air at temperatures above 250 °C. Since samples with the best morphology and structure were obtained when starting concentrations were 0.1 M $Zn(NO_3)_2$ and 1.0 M urea with hydrothermal reaction at 120 °C for 6 h and the subsequent annealing at 400 °C for 2 h, the samples for structure analysis and optical measurements were fabricated following these conditions without special mention.

Characterization. Powder XRD patterns for phase purity identification were collected on Philips X'pert PRO diffractometer with Cu Kα radiation, step size 0.0335°. High-resolution XRD patterns for Rietveld refinement were collected on HUBER Imaging Plate Guinier camera G670[S], Cu Kα1 radiation, Ge monochromator, step size 0.005°. Micromorphologies, microstructures, and element analysis were carried out on field-emission scanning electron microscope (FESEM, Sirion 200), transmission electron microscope (TEM, JEOL 2010, 200 kV),

* To whom correspondence should be addressed. Telephone: 086-0551-5591420. Fax: 086-0551-5591434. E-mail: xyzeng@issp.ac.cn; ldzhang@issp.ac.cn.
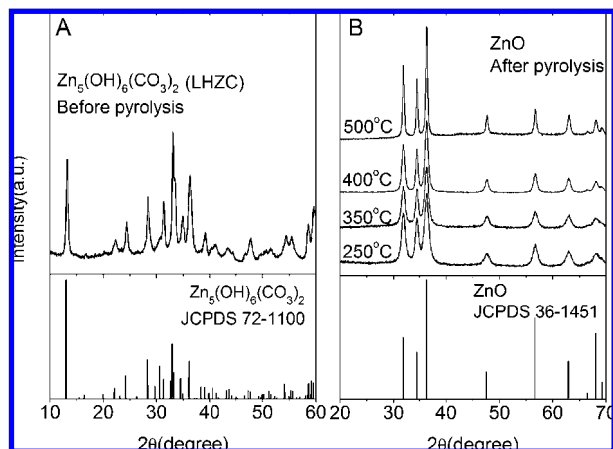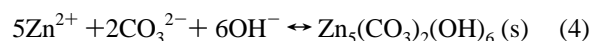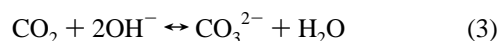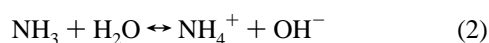† Shanghai Institute of Ceramics, Chinese Academy of Sciences.

Figure 1. XRD patterns of hydrothermal precipitate (A) before and (B) after heat treatment at different temperatures for 2 h in air.

and energy dispersive X-ray (EDX) accessory of the TEM. The room-temperature emission and excitation spectra were recorded with a Fluorolog-3 Jobin Yvon spectrophotometer equipped with a 450 W Xe lamp as the excitation source and a Hamamatsu R928 PMT to record the signals.

3. Results and Discussion

3.1. Morphology and Structure. Urea as a homogeneous precipitation agent has been widely exploited in synthesizing metal oxide nanostructures, of which the kinetics of nucleation, growth, and thus the morphology and structure of particles could be controlled by adjusting specimen concentration, reaction time, and temperature.[9,10] The decomposition of urea can produce OH^- anions and CO_3^{2-} anions, which would form precipitates with Zn^{2+} cation, such as hydrolyzed zinc carbonate and zinc carbonate. OH^- ions are formed as a result of reaction of NH_3 with H_2O, and CO_3^{2-} is produced by the reaction of CO_2 with OH^-:

$$CO(NH_2)_2 + H_2O \leftrightarrow CO_2 + 2NH_3 \quad (1)$$

$$NH_3 + H_2O \leftrightarrow NH_4^+ + OH^- \quad (2)$$

$$CO_2 + 2OH^- \leftrightarrow CO_3^{2-} + H_2O \quad (3)$$

$$5Zn^{2+} + 2CO_3^{2-} + 6OH^- \leftrightarrow Zn_5(CO_3)_2(OH)_6 \text{ (s)} \quad (4)$$

As shown in the powder XRD patterns (Figure 1), the hydrothermal precipitate is layered hydrolyzed zinc carbonate (LHZC), $Zn_5(OH)_6(CO_3)_2$, which can be pyrolysized into pure hexagonal ZnO phase after subsequent annealing (>250 °C) in air. The size of the obtained ZnO nanoparticles increases as the annealing temperature increases. For instance, the diameters of ZnO nanoparticles estimated from the Scherrer formula are 10, 11, 14, 24, and 32 nm when the annealing temperatures are 250, 350, 400, 500, and 700 °C, respectively. As revealed by SEM images (Figure 2), the hydrothermal precipitates are hierarchical microspheres that are constructed by single-crystalline nanosheets with thickness of 10−25 nm closely stacking into cabbagelike microspheres with diameters within 5−25 μm (Figure 3). The structure of the nanosheet and hierarchical sphere is retained in the subsequent annealing in air, during which the single-crystalline LHZC nanosheets function as the self-template for the formation of ZnO nanosheets that aggregated into cabbagelike microspheres (Figure 2C).
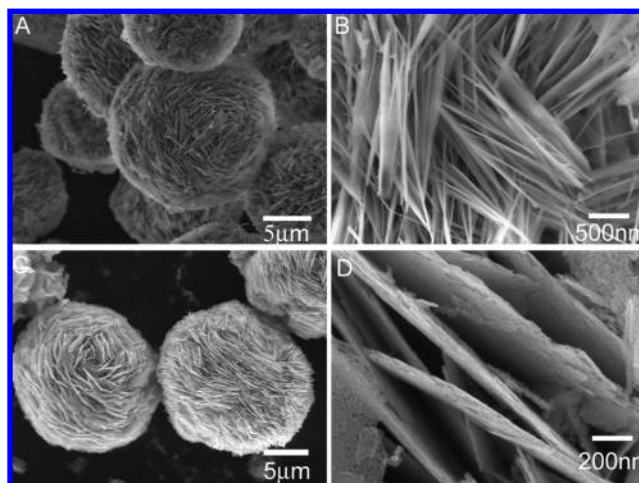

Figure 2. (A) FESEM image of nanosheet aggregated microspheres of $Zn_5(OH)_6(CO_3)_2$ (LHZC). (B) Side view of the nanosheets of LHZC that construct the microspheres. (C) FESEM image of microspheres of ZnO that were obtained after annealing at 400 °C for 2 h. (D) Side view of the mesoporous nanosheets of ZnO that construct the microsphere of ZnO.
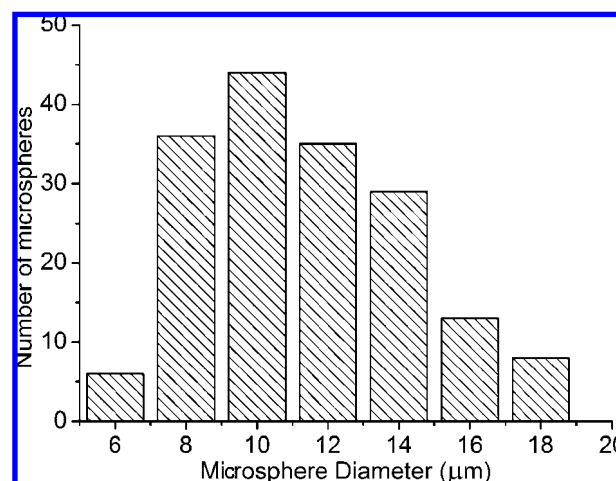

Figure 3. Diameter distribution (sample size 171 microspheres) of the LHZC microspheres.

However, as revealed in Figure 2D the obtained ZnO nanosheets are mesoporous, which could be attributed to the loss of volatile gas such as H_2O and CO_2 during the heat treatment. Similar hierarchical spheres have been observed in various oxide systems, such as YBO_3,[11] MgO,[12] Fe_2O_3,[13] copper hydroxide,[14] and $Fe_2(MoO_4)_3$.[15]

TEM analysis shown in Figure 4 provided further structural information about LHZC nanosheets and the ZnO nanosheet. The LHZC nanosheet, which extends in the plane of *b*- and *c*-axes, is of single-crystalline quality (Figure 4A and inset). Fast moving ions in LHZC, such as CO_3^{2-} and OH^-, can be easily released during heat treatment or under the bombardment of incident high-energy electron beam. In the high-resolution TEM (HRTEM) mode, LHZC nanosheets quickly decompose into ZnO polycrystalline sheets that are composed of ZnO nanocrystals with diameters of 3−6 nm (Figure 4B). The ZnO nanosheets after heat treatment at 400 °C for 2 h in air are of quasi-single-crystalline quality, except that irregular mesopores with diameters of 10−30 nm also appear during the pyrolysis process (Figure 4C). The mesopores in the nanosheet might come from the Kirkendall effect, in which the vacancies that
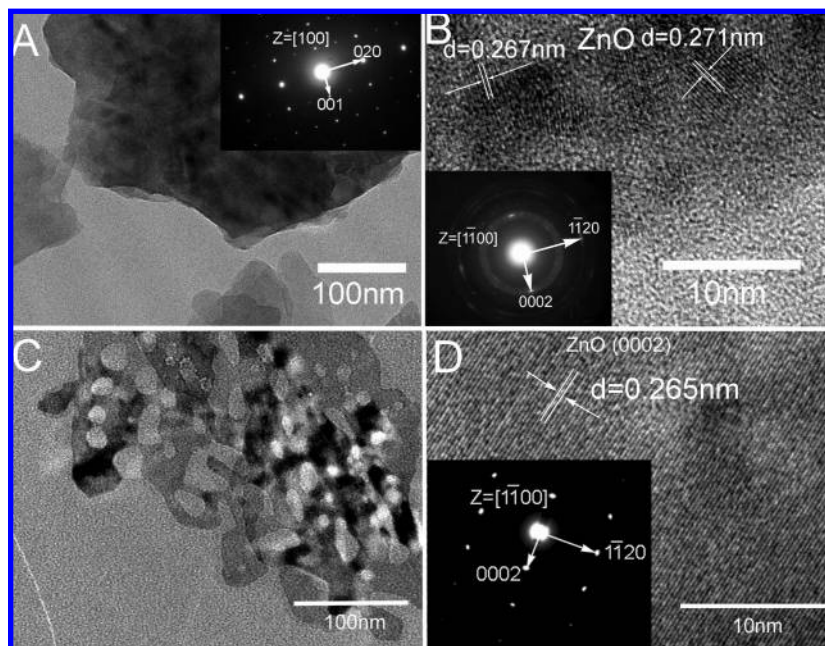
ZnO Microspheres and Rare Earth Doped Luminescence

J. Phys. Chem. C, Vol. 112, No. 10, 2008 **3505**

Figure 4. TEM images of nanosheets before and after pyrolysis. (A) LHZC nanosheets before pyrolysis with the typical SAED of LHZC monolayer in the inset. (B) HRTEM image of LHZC nanosheet that can readily decompose into ZnO nanocrystalline sheet under the bombardment of high-energy electrons, and the inset is SAED of the nanocrystalline sheet of ZnO. (C) Porous quasi-single-crystalline nanosheet of ZnO after annealing at 400 °C for 2 h. (D) HRTEM and SAED images of the ZnO quasi-single-crystalline nanosheet.

balance the released molecules (H_2O, CO_2) can condense to form voids in the nanosheet.[16] In the HRTEM image of the ZnO nanosheet (Figure 4D), dislocations and stacking faults are rarely observed, and the clear lattice fringes with spacing of 0.267 nm between adjacent lattice planes correspond to the *d*-spacing of (0002) plane of ZnO. By indexing the SAED inserted in Figure 4D, it was found that the quasi-single-crystalline nanosheet of ZnO extends in the plane of [001] and [110] axis and most of the surface belongs to the nonpolar ($1\bar{1}00$) crystal plane of wurtzite ZnO. Moreover, considering the matched *d*-spacing between the (002) planes of ZnO and $Zn_5(OH)_6$-$(CO_3)_2$, the $Zn_5(OH)_6(CO_3)_2 \rightarrow$ ZnO solid-state conversion is topotactic, which might help explain the formation of quasi-single-crystalline ZnO nanosheets.[17] Anyway, the ZnO nanosheet with the *c*-axis in the sheet is rarely reported.[18] Since optical properties of ZnO nanostructures are highly morphology related,[3] such hierarchical microspheres constructed by mesoporous quasi-single-crystalline ZnO nanosheets would exhibit novel optical properties distinct from that of ZnO nanorods and nanowires.

In the fabrication of rare earth ion (RE^{3+}) doped ZnO samples, the successful doping of RE^{3+} ions into ZnO mesoporous nanosheets can be proved by EDX spectra of single ZnO:RE nanosheet (Figures 5A and S1 in Supporting information) and lattice expansion obtained from Rietveld refinement of high-resolution XRD patterns (Figure 5B). Rietveld refinement was carried out using the *FullProf* software package.[19] Because of the similarities in chemical behavior among lanthanide series, only Eu^{3+} is presented here as an example. The unit cell volume of ZnO:1%Eu is 0.14% larger than that of undoped ZnO sample. The doping concentration was kept as low as 0.3% to avoid the appearance of hydrolyzed rare earth carbonate.

3.2. Time Evolution and Growth Mechanism of LHZC Microspheres. As shown in Figure 6, LHZC crystallizes in a layered behavior in the (100) plane, in which the [ZnO_6] octahedra and [ZnO_4] tetrahedra connect with each other to form a close stacking layer, and the neighboring zinc oxide layers are combined by weak CO_3^{2-} and OH^- anions.[20] Hence, the
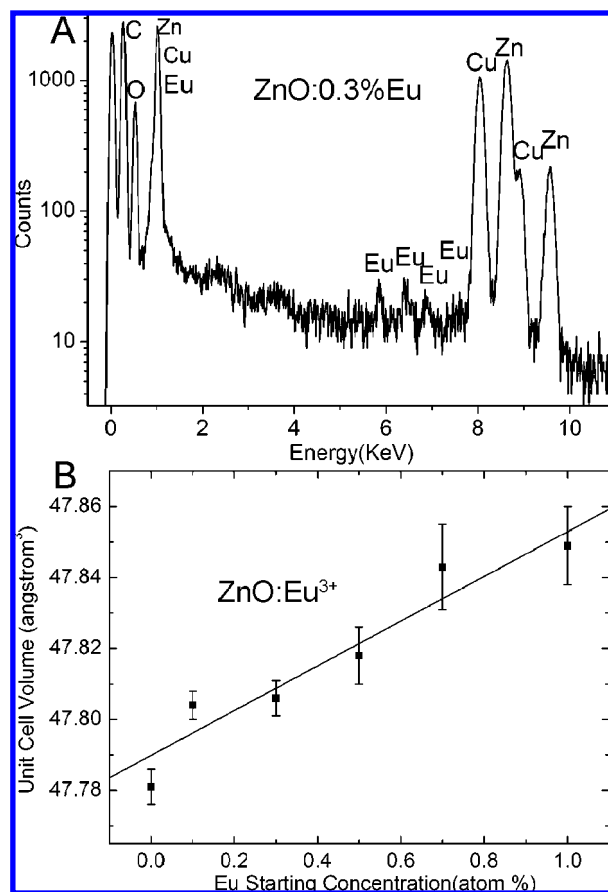

Figure 5. (A) Typical EDX spectra of a single ZnO:Eu nanosheet in a ZnO:0.3%Eu sample. (B) Unit cell volume of ZnO:Eu as a function of starting concentration of Eu^{3+}. The values were obtained from Rietveld refinement of high-resolution XRD patterns of ZnO:*x*%Eu^{3+} (*x* = 0, 0.1, 0.3, 0.5, 0.7, 1.0) samples.

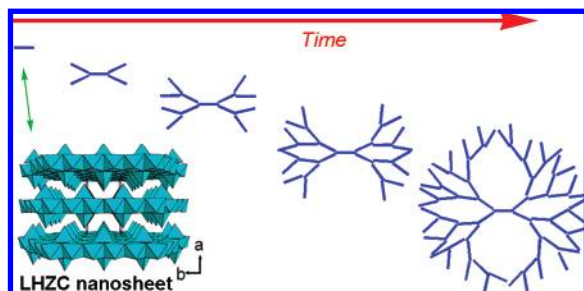nucleation and growth of the crystalline LHZC nanosheet are more likely to happen at the edge of each nanosheet, which

3506 *J. Phys. Chem. C, Vol. 112, No. 10, 2008*

Zeng et al.

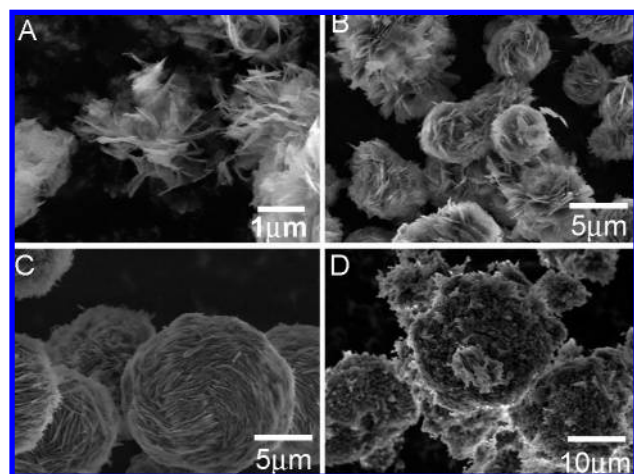**Figure 6.** Scheme of growth mechanism of LHZC microspheres in the hydrothermal process.

Figure 7. SEM image LHZC microspheres after hydrothermal treatment at 120 °C for (A) 1, (B) 1.5, (C) 6, and (D) 24 h. The starting concentrations are 0.1 M for $Zn(NO_3)_2$ and 1.0 M for urea.

Figure 8. FESEM images of hydrothermal products with different starting concentrations of $Zn(NO_3)_2$ and urea: urea 1 M and Zn^{2+} 0.02, 0.06, and 0.25 M for A, B, and C, respectively; Zn^{2+} 0.1 M and urea 0.2, 1, and 2 M for D, E, and F, respectively. In the experiments, the samples were held at 120 °C for 6 h.

would lead to the morphological evolution of a single nanosheet → dumbbell-like aggregate → cabbagelike sphere, which are presented schematically along the time arrow in Figure 6.

The proposed growth mechanism of LHZC hierarchical microspheres was verified by comparing the morphologies of hydrothermal products after different reaction times (Figure 7). When the reaction time is as short as 1 h, only loosely aggregated clusters of nanosheets were obtained, which could be regarded as being at the early stages of growth of LHZC microsphere. The clusters start to grow into cabbagelike hierarchical microspheres when the hydrothermal reaction time was extended to 1.5 h. Larger cabbagelike microspheres with more regular shape and more compact nanosheets could be obtained if the hydrothermal time is prolonged, for instance, 4−10 h. LHZC microspheres with the best morphology and crystalline quality could be obtained at 120 °C with hydrothermal time of 6 h. Under hydrothermal conditions, nucleation, crystal growth, and Ostwald ripening are decisive processes in the formation of regular shaped hierarchical microspheres. Nevertheless, further prolonging the hydrothermal time, for example, 24 h, would deteriorate the morphology of LHZC microspheres, in which part of the LHZC nanosheets have been disaggregated and converted into the more stable zinc carbonate phase (Figure 7D).

3.3. Starting Concentration and Morphology of LHZC Microspheres. In addition to reaction time, concentrations of $Zn(NO_3)_2$ and urea are also decisive parameters in the formation of LHZC microspheres. To clarify the effects of starting concentrations, a systematic comparison was made by varying the starting concentrations of $Zn(NO_3)_2$ and urea. First, the starting concentration of urea was kept at 1.0 M and the concentration of $Zn(NO_3)_2$ was 0.02, 0.06, and 0.25 M, from
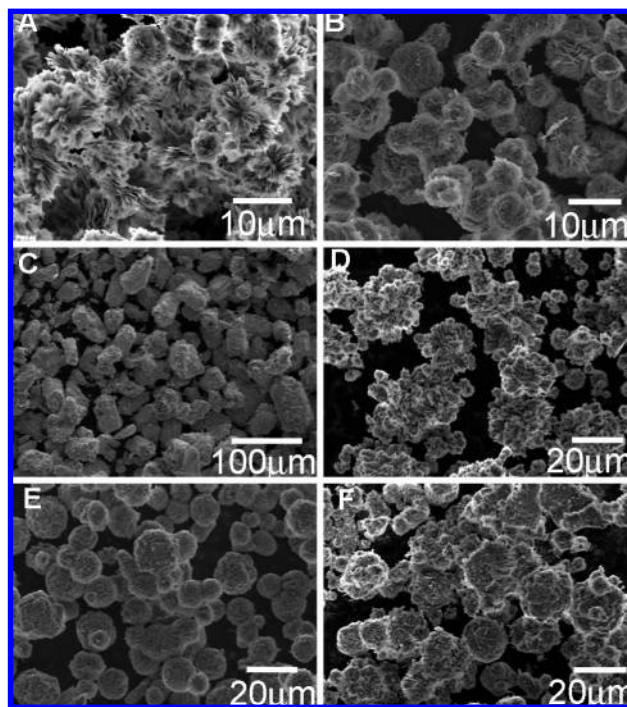
which the SEM images of hydrothermal products were shown in Figure 8A−C, respectively. Then the concentration of $Zn(NO_3)_2$ was kept at 0.10 M and the concentration of urea was 0.2, 1.0, and 2.0 M, of which SEM images were presented in Figure 8D−F, respectively. As shown in Figure 8A,D, low concentration of either $Zn(NO_3)_2$ or urea will lead the formation of irregular dumbbell-like aggregates of LHZC nanosheets, because renucleation of a new LHZC nanosheet at the edge of an original LHZC nanosheet is prohibited because of undersaturation of reacting ions in low concentration conditions. In contrast, high concentration of either $Zn(NO_3)_2$ or urea would result in the emergence of the more stable $ZnCO_3$ phase. For example, in Figure 8C with 0.25 M $Zn(NO_3)_2$ and 1.0 M urea as starting materials, irregular blocklike $ZnCO_3$ particles were obtained. In Figure 8F with 0.1 M $Zn(NO_3)_2$ and 2.0 M urea, part of the LHZC nanosheets have been converted to $ZnCO_3$, which is similar to the situation in Figure 7D. The high starting concentrations promote the dissolution of the LHZC nanosheets and the emergence of the more stable precipitates $ZnCO_3$. According to the proposed growth mechanism discussed above (Figure 6), moderate concentrations of reaction ions are required to provide an appropriate balance between nucleation and growth of the LHZC nanosheets, which is crucial to the formation of spherical aggregates of the LHZC nanosheets. In conclusion, the LHZC nanosheets aggregated hierarchical microspheres with the best crystalline quality can be obtained with moderate starting concentrations of zinc nitrate (0.1 M) and urea (1.0 M) and hydrothermal reaction at 120 °C for 6 h.

3.4. Photoluminescent Properties of Rare Earth Doped ZnO. In the experiments, doping with a small amount of rare earth nitrates would not yield a notable morphological difference; hence, in the fabrication of undoped and rare earth doped ZnO samples for optical measurements the starting concentration of $Zn(NO_3)_2$ and urea was kept at 0.1 and 1.0 M, respectively, and the doping concentration of rare earth ions was kept at 0.3%

ZnO Microspheres and Rare Earth Doped Luminescence
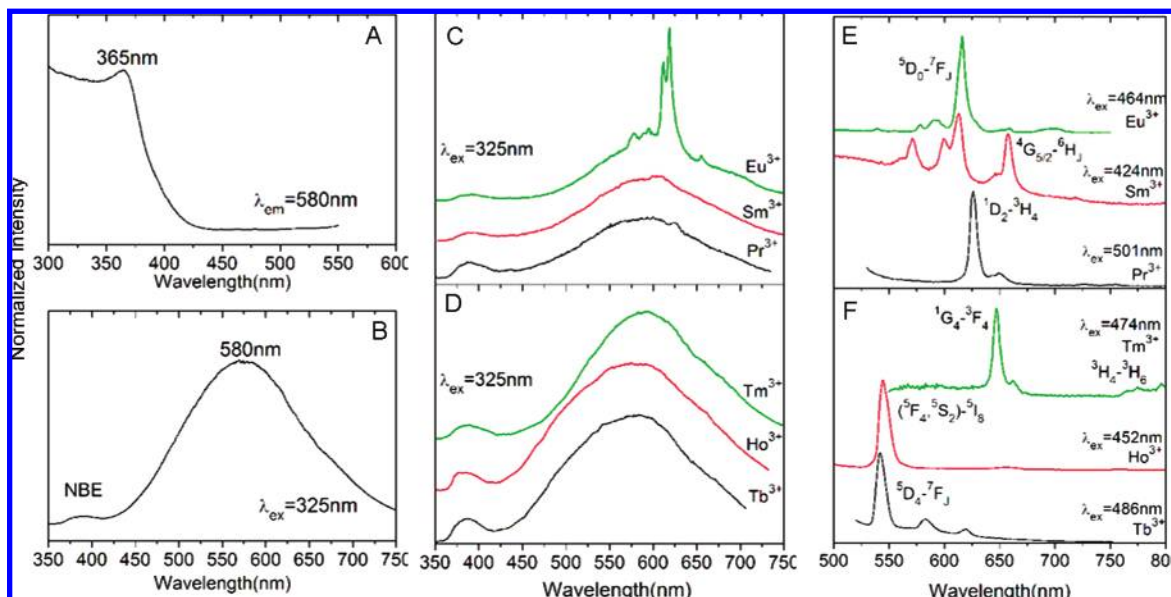
J. Phys. Chem. C, Vol. 112, No. 10, 2008 **3507**

Figure 9. Room-temperature photoluminescence spectra of undoped and rare earth RE^{3+} (0.3% atom) doped ZnO samples. (A, B) Excitation and emission spectra of undoped ZnO sample. (C, D) UV-excited emission spectra of ZnO:RE^{3+} samples. (E, F) 4f−4f excited emission spectra of RE^{3+} ions in ZnO:RE^{3+} samples. The spectra curves in C, D, E, and F have been lifted vertically for display clarity.

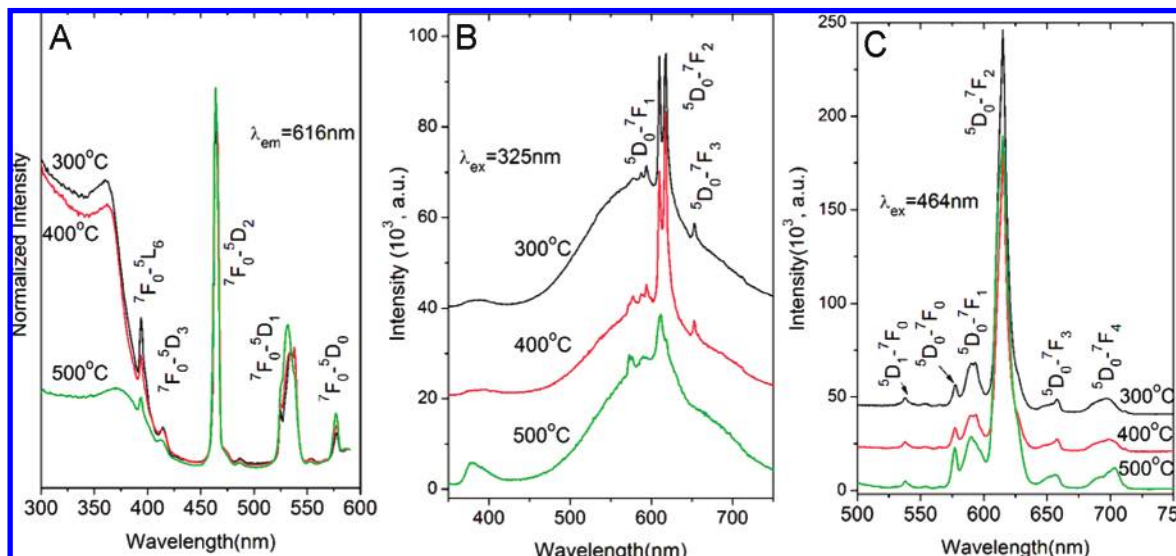**Figure 10.** Room-temperature photoluminescence spectra of ZnO:0.3%Eu^{3+} samples annealed at different temperatures for 2 h in air. (A) Excitation spectra monitoring Eu^{3+} emission at 616 nm. (B) Emission spectra under UV excitation. (C) Emission spectra of Eu^{3+} under the direct $^7F_0-^5D_2$ excitation at 464 nm. The curves in A are normalized at 464 nm, and the curves in B and C have been lifted vertically for display clarity.

(atom) to avoid the emergence of excess RE^{3+} ions outside of the ZnO nanosheets. The successful doping of RE^{3+} into the ZnO nanosheet has already been proved by EDX spectra and lattice expansion (Figures 5 and S1 in Supporting information). As shown in Figure 9A,B, the UV photon-excited emission spectra of undoped ZnO sample are characterized by a weak near band edge emission (NBE) at 380 nm and a broad band at 580 nm (FWHM 160 nm) that is attributed to interstitial oxygen in ZnO lattice.[21] UV photon with wavelength shorter than the band edge (λ < 365 nm) can be absorbed and generate one electron−hole pair in ZnO nanostructure. In previously reported studies of rare earth ion doped ZnO systems, no energy transfer from photon-generated electron−hole pairs to rare earth centers could be observed.[6] In our experiments, when the ZnO samples singly doped with RE^{3+} (RE = Pr, Sm, Tb, Ho, and Tm) were excited by UV photons (λ < 365 nm), there was no notable characteristic 4f−4f emissions of doped RE^{3+} ion either, which ruled out ZnO → RE^{3+} energy transfer (Figure 9C,D). However,

the 4f−4f emissions of doped RE^{3+} ions could be observed when the RE^{3+} ions were excited at wavelengths that were resonant with their 4f−4f transitions (Figure 9E,F). The absence of ZnO → RE^{3+} energy transfer could be attributed to the quenching effect of defect-related emission and the inappropriate energy level positions of RE^{3+} relative to the VB and CB of ZnO.[8]

In contrast, in the Eu^{3+}-doped ZnO sample the ZnO → Eu^{3+} energy transfer was evidently observed. As shown in Figure 9C, under the excitation of UV photon of 325 nm, the $^5D_0-^7F_J$ ($J = 0-3$) emission of Eu^{3+} with moderate intensity was clearly recorded, together with the weak NBE emission and defect-related broad emission of ZnO. More details of the photoluminescent spectra of ZnO:Eu^{3+} are presented in Figure 10, in which the excitation spectra, UV-excited emission spectra, and 464-nm excited emission spectra of ZnO:Eu^{3+} samples annealed at different temperatures (300, 400, and 500 °C) are illustrated together. The excitation spectra consist of two parts: the sharp

lines at 394, 414, 464, and 531 nm that correspond to the intrinsic 4f–4f transitions of Eu^{3+} and a broad band that resembles the excitation spectrum of undoped ZnO, of which the latter one corresponds to a delocalized excitation mechanism (i.e., the photon-generated delocalized electron–hole pairs transfer energy to Eu^{3+} ions). The UV-excited Eu^{3+} emission is characterized by a doublet splitting of $^5D_0$–$^7F_2$ emission at 612 and 619 nm, whereas the 464-nm excited Eu^{3+} emission features one sharp peak of $^5D_0$–$^7F_2$ at 616 nm and weak emission from the second lowest excited level at 539 nm ($^5D_1$–$^7F_0$), which suggests that the emitting Eu^{3+} ions in the two excitation situations are located at different sites in the ZnO nanosheet. As discussed below, the UV-excited emitting Eu^{3+} ions are located at the surface layer of the ZnO nanosheets, and the other Eu^{3+} ions are in the inner part of the ZnO nanosheet where the crystal lattice resembles that of bulk ZnO crystal.

As shown in Figure 10B, increasing the subsequent annealing temperature to 500 °C would significantly reduce the intensity and change the splitting behavior of the UV-excited Eu^{3+} emissions, but would bring about little change in the 464-nm excited emissions. Verified by the sharper peaks in the XRD pattern (Figure 1B) and stronger NBE emission around 380 nm (Figure 10B), the grain growth process is evident during the heat treatment at 500 °C, which leads to the reduction of nanocrystal surface and consequently the reduction of surface defects that can trap and transfer energy to Eu^{3+} ions. However, higher annealing temperature does not bring about apparent changes in the 464-nm excited Eu^{3+} emission (Figure 10C), which could be explained by the stable local coordination environment of Eu^{3+} ion in the inner part of the ZnO nanosheets.

It is noteworthy that the observed UV-excited Eu^{3+} emission could not originate from possible Eu^{3+}-containing phases outside of the ZnO nanosheets, such as hydroxide europium carbonate, europium carbonate, or europium hydroxide. The observation of the ZnO absorption band ($\lambda < 365$ nm) undoubtedly verifies the efficient energy transfer from electron–hole pairs in the ZnO nanosheet to Eu^{3+}, which is unlikely to occur if the Eu^{3+} ions are out of the ZnO nanosheet. The observation of ZnO → Eu^{3+} energy transfer in this work is very extraordinary since there was no evident energy transfer in the previously reported Eu^{3+} singly doped ZnO systems, such as bulk single crystal, ceramic, nanowire, or nanoparticles.[6] It is established that Eu^{3+} emission always relates to charge-transfer state and the ground-state energy level of Eu^{2+} should be below the bottom of CB.[22] In the surface layer of the mesoporous quasi-single-crystalline ZnO nanosheet, the ground-state energy level of Eu^{2+} might be just below the bottom of CB because of the defect-induced band upward bending of both CB and VB.[23] As a result, the ground-state level of Eu^{2+} in the surface level may function as a stable trap level for the intermediate efficient ZnO → Eu^{3+} energy transfer.

4. Conclusions

We have demonstrated the fabrication of hierarchical ZnO microspheres by pyrolysis of the hydrothermally obtained Zn_5-$(CO_3)_2(OH)_6$ (LHZC) microspheres, which are constructed by single-crystalline LHZC nanosheets. The regular hierarchical microspheres of LHZC are obtained by hydrothermal precipitation at 120 °C for 6 h with appropriate concentrations of Zn-$(NO_3)_2$ and urea. A possible growth mechanism of LHZC microspheres is proposed. In the subsequent pyrolysis process, single-crystalline LHZC nanosheets decompose into mesoporous quasi-single-crystalline ZnO nanosheets.

Under the UV excitation from a 450 W Xe lamp, ZnO microspheres show a weak near band edge emission around 380 nm and a yellow band around 580 nm that is related to oxygen interstitial defects. When the samples are doped with trivalent rare earth ion, RE^{3+} (RE = Pr, Sm, Tb, Ho, Tm), no ZnO → RE^{3+} is observed. However, when Eu^{3+} is doped, efficient Eu^{3+} emissions are recorded under UV photon excitation ($\lambda < 365$ nm), which is attributed to energy transfer from photon-generated electron–hole pair in the ZnO nanosheet to Eu^{3+} in the surface layer of the ZnO nanosheet.

Supporting Information Available: Typical EDX spectra of a single ZnO:RE nanosheet. This material is available free of charge via the Internet at http://pubs.acs.org.

References and Notes

(1) (a) Baer, E.; Hiltner, A.; Keith, H. D. *Science* **1987**, *235*, 1015. (b) Kuang, D.; Brezesinski, T.; Smarsly, B. *J. Am. Chem. Soc.* **2004**, *126*, 10534. (c) Gao, J.; Yu, A.; Itkis, M. E.; Bekyarova, E.; Zhao, B.; Niyogi, S.; Haddon, R. C. *J. Am. Chem. Soc.* **2004**, *126*, 16698. (d) Chaudhary, S.; Lu, H.; Muller, A. M.; Bardeen, C. J.; Ozkan, M. *Nano Lett.* **2007**, *7*, 1973.

(2) (a) Service, R. F. *Science* **1997**, *276*, 895. (b) Liu, C.; Zapien, J. A.; Yao, Y.; Meng, X.; Lee, C. S.; Fan, S.; Lifshitz, Y.; Lee, S. T. *Adv. Mater.* **2003**, *15*, 838. (c) Tsukazaki, A.; Ohtomo, A.; Onuma, T.; Ohtani, M.; Makino, T.; Sumiya, M.; Ohtani, K.; Chichibu, S. F.; Fuke, S.; Segawa, Y.; Ohno, H.; Koinuma, H.; Kawasaki, M. *Nat. Mater.* **2005**, *4*, 42.

(3) Shalish, I.; Temkin, H.; Narayanamurti, V. *Phys. Rev. B* **2005**, *69*, 245401.

(4) Wang, Y. D.; Zang, K. Y.; Chua, S. J.; Fonstad, C. G. *Appl. Phys. Lett.* **2006**, *89*, 263116.

(5) (a) Steckl, A. J.; Heikenfeld, J. C.; Munasinghe, C.; Lee, D. S.; Wang, Y. Q.; Jones, R. *2003 IEEE LEOS Annual Meeting Conference Proceedings* **2003**, *2*, 656. (b) Andreev, B. A.; Krasilnik, Z. F.; Kryzhkov, D. I.; Kuznetsov, V. P.; Gregorkiewicz, T.; Jantsch, W. *Appl. Phys. Lett.* **2006**, *88*, 201101.

(6) (a) Bhargava, R. N.; Chhabra, V.; Som, T.; Ekimov, A.; Taskar, N. *Phys. Status Solidi B* **2002**, *229*, 892. (b) Abdullah, M.; Morimoto, T.; Okuyama, K. *Adv. Funct. Mater.* **2003**, *13*, 800. (c) Ishizumi, A.; Kanemitsu, Y. *Appl. Phys. Lett.* **2005**, *86*, 253106. (d) Gao, S.; Zhang, H.; Deng, R.; Wang, X.; Sun, D.; Zheng, G. *Appl. Phys. Lett.* **2006**, *89*, 123125.

(7) Kelly, A.; Groves, G. W. *Crystallography and Crystal Defects*; Addison-Wesley: Reading, MA, 1970.

(8) (a) Dorenbos, P.; van der Kolk, E. *Appl. Phys. Lett.* **2006**, *89*, 061122. (b) Dorenbos, P.; van der Kolk, E. *Proc. SPIE-Int. Soc. Opt. Eng.* **2007**, *6473*, 647313.

(9) Yan, C.; Xue, D. *J. Phys. Chem. B* **2006**, *110*, 11076.

(10) Hosono, E.; Fujihara, S.; Honma, I.; Zhou, H. *Adv. Mater.* **2005**, *17*, 2091.

(11) Jiang, X.-C.; Sun, L.-D.; Yan, C.-H. *J. Phys. Chem. B* **2004**, *108*, 3387.

(12) Yan, C.; Xue, D. *J. Phys. Chem. B* **2005**, *109*, 12358.

(13) Zhou, L.-S.; Hu, J.-S.; Liang, H.-P.; Cao, A.-M.; Song, W.-G.; Wang, L.-J. *Adv. Mater.* **2006**, *18*, 2426.

(14) Zhang, Z.; Shao, X.; Yu, H.; Wang, Y.; Han, M. *Chem. Mater.* **2005**, *17*, 332.

(15) Ding, Y.; Yu, S.-H.; Liu, C.; Zang, Z.-A. *Chem.–Eur. J.* **2007**, *13*, 746.

(16) Smigelskas, A. D.; Kirkendall, E. O. *Trans. AIME* **1947**, *171*, 130.

(17) Li, Y.; Tan, B.; Wu, Y. *J. Am. Chem. Soc.* **2006**, *128*, 14258.

(18) Kong, X. Y.; Ding, Y.; Yang, R. S.; Wang, Z. L. *Science* **2004**, *303*, 1348.

(19) Rodriguez-Carvajal, J. *FullProf*; Institut Laue-Langevin: Grenoble, France, July 2006.

(20) Ghose, S. *Acta Crystallogr.* **1964**, *17*, 1051.

(21) Hsu, J. W. P.; Tallant, D. R.; Simpson, R. L.; Missert, N. A.; Copeland, R. G. *Appl. Phys. Lett.* **2006**, *88*, 252103.

(22) Dorenbos, P. *J. Phys.: Condens. Matter* **2003**, *15*, 8417.

(23) Bachir, S.; Azuma, K.; Kossanyi, J.; Valat, P.; Ronfard-Haret, J. C. *J. Lumin.* **1997**, *75*, 35.